Strongly enhanced temperature dependence of the chemical potential in FeSe

L. C. Rhodes,[1,2] M. D. Watson,[2] A. A. Haghighirad,[3] M. Eschrig,[1] and T. K. Kim[2]

[1]*Department of Physics, Royal Holloway, University of London, Egham, Surrey TW20 0EX, United Kingdom*
[2]*Diamond Light Source, Harwell Campus, Didcot OX11 0DE, United Kingdom*
[3]*Clarendon Laboratory, Department of Physics, University of Oxford, Parks Road, Oxford OX1 3PU, United Kingdom*

Employing a 10-orbital tight-binding model, we present a set of hopping parameters fitted directly to our latest high-resolution angle-resolved photoemission spectroscopy (ARPES) data for the high-temperature tetragonal phase of FeSe. Using these parameters, we predict a large 10 meV shift of the chemical potential as a function of temperature. To confirm this large temperature dependence, we performed ARPES experiments on FeSe and observed a ∼25 meV rigid shift to the chemical potential between 100 and 300 K. This strong shift has important implications for theoretical models of superconductivity and of nematic order in FeSe materials.

I. INTRODUCTION

To understand high-temperature superconductivity and nematic order in iron-based superconductors, it is necessary to obtain an accurate description and understanding of their electronic structure. However, modeling the electronic structure of iron-based superconductors has proved to be a challenging task. *Ab initio* calculations such as density functional theory (DFT) show some disagreement with quantum oscillation experiments [1], as well as with the band dispersions obtained from angle-resolved photoemission spectroscopy (ARPES) [2,3]. In fact, the calculated models need to be renormalized by a factor between 2 and 10 to be in qualitative agreement with experimental results [4]. More sophisticated theoretical treatments such as dynamical mean-field theory (DMFT) are able to account for the orbital-dependent band renormalizations [5], yet they do not account for more specific features, such as the shrinking of the hole and electron pockets seen in even the simplest iron-based superconductor, FeSe [6].

FeSe has attracted a lot of interest due to the highly tuneable nature of the superconducting transition temperature, ranging from 8 K in bulk samples [7], 37 K under pressure [8], 43 K with intercalation [9], and 65 K with a monolayer grown on $SrTiO_3$ [10]. At 90 K, bulk FeSe also experiences a nematic transition: a form of electron correlation that breaks fourfold rotational symmetry [11], yet unlike most other iron-based superconductors, it is not accompanied by an antiferromagnetic phase transition. In recent years, ARPES studies on FeSe have yielded increasingly detailed information on the quasiparticle dispersions [12–16], however despite the theoretical interest, a fully accurate model consistent with experiment is still lacking.

In this paper, we present a set of tight-binding parameters fitted directly to experimental data for the high-temperature tetragonal phase of FeSe. Our parameters are optimized against high-resolution ARPES data at 100 K, and provide a quantitatively accurate description of the observed three-dimensional (3D) electronic structure. Using this parameter set, we predict a large 10 meV rigid increase of the chemical potential between 100 and 300 K, not predicted from a DFT-based parameter set. Motivated by this finding, we have also performed a temperature-dependent ARPES study on FeSe up to 300 K, and observed an enhanced chemical potential shift of ∼25 meV. We discuss a possible explanation for this enhancement of the observed chemical potential shift with respect to the model prediction. Our results highlight the crucial importance of complete consideration of the chemical potential in both theory and experiment.

II. EXPERIMENTAL METHODS

High-quality single-crystal samples of FeSe were grown by chemical vapor transport [17]. ARPES measurements were performed at the I05 beamline at the Diamond Light Source, UK [18]. The Fermi level was calibrated by fitting the Fermi function to freshly deposited polycrystalline gold at 35 K. All maps and band dispersions presented here were measured with a photon energy of 56 eV. This ensured that only a single reference measurement from the polycrystalline gold was needed to calibrate the binding energy, eliminating a possible source of experimental error.

Band dispersions used for the optimization of the tight-binding model were taken from data published in Refs. [13,14] by fitting a Lorentzian to the momentum distribution curves (MDC) at 100 K for photon energies of 37 eV ($k_z = 0$) for the Γ and M points and 56 eV ($k_z = \pi/c$) for the Z and A points.

III. TIGHT-BINDING MODEL

We use the 10-orbital tight-binding model of Ref. [19] with the inclusion of an additional spin-orbit coupling term [20] as the framework for our phenomenological optimization. This model includes all 10 d-orbitals associated with the $P4/nmm$ crystallographic space group, i.e., the 2-Fe unit cell.

Several previous tight-binding models [21,22] have used the glide symmetry of the 2-Fe unit cell to unfold the Brillouin zone into a **k**-space corresponding to a 1-Fe unit cell [23]. While the 1-Fe and 2-Fe unit-cell descriptions are exactly equivalent with the exclusion of spin-orbit coupling, it has been shown that the 2-Fe unit-cell representation is required
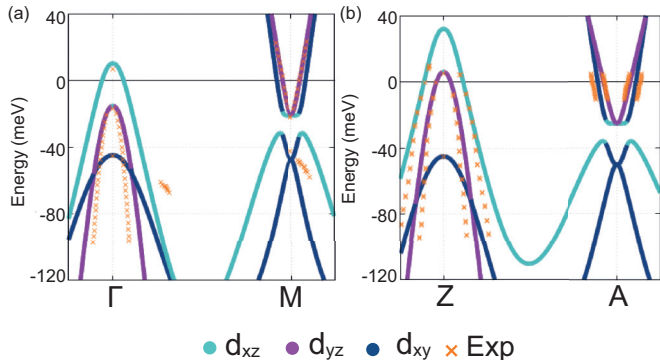
FIG. 1. Band dispersions calculated from the tight binding model with our ARPES-based parameters, shown for $k_z = 0$ (a) and $k_z = \pi$ (b), together with experimental data points used to constrain the model (orange crosses).

in the presence of spin-orbit coupling [24,25]. Therefore, optimization of our parameter set against experimental ARPES data with sizable spin-orbit coupling [12] requires a full 2-Fe unit-cell treatment.

In Fig. 1 we show the calculated band structure obtained using our phenomenological tight-binding parameters fitted to ARPES data obtained in the high-temperature tetragonal phase at 100 K. We present our ARPES-based parameters in the Appendix. These parameters were optimized at both $k_z = 0$ (Γ and M) and $k_z = \pi$ (Z and A), providing a complete three-dimensional description of the electron structure of FeSe.

The addition of the spin-orbit interaction term manifests itself in two ways. First, it lifts the degeneracy of the d_{xz} and d_{yz} bands revealing a 20 meV splitting at Γ and Z [12], and secondly, it creates an anticrossing of the d_{xy} and d_{xz} bands near the M and A points. The parameters also correctly describe the recently observed separation at the M and A points [14,15] between the degenerate d_{xz}/d_{yz} band at -22 meV and the d_{xy} band at -42 meV. In the ARPES data there is also a d_{z^2} band at ~ -220 meV, which is accounted for in the model, although not shown.

In this tight-binding model, the size of the electron pocket and flatness of the d_{xy} band are controlled by the same hopping parameters. Since we wish to maintain quantitative agreement at the Fermi surface, it became necessary to have an exaggerated d_{xy} dispersion at higher energies. Nevertheless, the binding energies of the bands at the high-symmetry points are in agreement with experiment, as are the dispersion of all the bands close to the chemical potential. Consequently, as the parameters were fitted within the region of -100 to $+10$ meV, we cannot comment on the reliability of the model at higher binding energies or in the unoccupied states.

This highly accurate description of the low-energy part of the band dispersions near the chemical potential allows us to quantitatively reproduce the experimentally determined Fermi surface. Our model therefore provides a good starting point for discussions of low-energy properties of FeSe.

IV. CHEMICAL POTENTIAL EFFECTS IN FeSe

Next we consider what turns out to be an important issue in FeSe, namely the temperature dependence of the chemical

potential. Temperature-dependent ARPES studies on the iron-based superconductors $BaFe_2As_2$ [26], $Ba(Fe_{1-x}Ru_x)_2As_2$ [27], and $FeSe_{1-x}S_x$ [28], as well as the semimetal WTe_2 [29], have all observed a substantial change of the k_F values of the hole and electron pockets, consistent with a rigid shift of the chemical potential as a function of temperature. This can be explained by the shallow nature of the hole and electron pockets in the iron-based superconductors, as discussed by Brouet *et al.* [26]. To maintain the total charge of the system, the chemical potential must shift to counterbalance any asymmetry in the density of electron and hole carriers as a function of an external variable such as temperature. This effect is small if the density of states around the chemical potential is uniform for both the hole and electron bands, such as in an unrenormalized DFT-based model. However, for the shallow band dispersions observed experimentally, with the top of the hole and bottom of the electron bands within a few $k_B T$ of the chemical potential, a change in temperature can have an anisotropic effect on the density of thermally active electron and hole carriers, necessitating a shift of the chemical potential.

A. Theoretical predictions

To determine the temperature evolution of the chemical potential in FeSe, we calculate the total number of electrons N,

$$N = 2 \sum_{\mathbf{k}} \sum_{\nu} f(E_\nu(\mathbf{k}) - \mu), \tag{1}$$

where ν is the band index, $E_\nu(\mathbf{k})$ is the energy of band ν at momentum $\mathbf{k}$, $f(E_\nu(\mathbf{k}) - \mu) = [1 + e^{\beta(E_\nu(\mathbf{k}) - \mu)}]^{-1}$ is the Fermi function with $\beta = \frac{1}{k_B T}$, and μ is the chemical potential. At 100 K the particle number was determined to be $12.00e^-$ for a $\mathbf{k}$-grid of size $64 \times 64 \times 8$. This is consistent with the total number of valence electrons available for two Fe^{2+} atoms in a 2-Fe unit cell. We fix N and calculate $\mu(T)$ from Eq. (1) numerically.

Figure 2(a) shows the results for the evolution of the chemical potential up to 300 K as predicted from the ARPES-based parameters. This is compared to the predicted evolution of the chemical potential using DFT-based parameters taken from Ref. [19]. While the DFT-based parameters would give rise to only a very small change of -0.4 meV between 100 and 300 K the ARPES based parameters predict a much larger 10 meV increase to the chemical potential.

In the case of the DFT-based parameters, the unrenormalized hole and electron bands crossing the chemical potential appear as large pockets with a wide bandwidth and relatively uniform density of states close to the chemical potential. Hence, the chemical potential hardly changes as a function of temperature, as would normally be the case in a metallic system. However, for the model based on the experimental band dispersions, much smaller Fermi surfaces and renormalized band dispersions close to the chemical potential are described, including a very shallow top of the hole band. Thus the thermal population of hole and electron states can become rather asymmetric, leading to a much more significant shift of the chemical potential. As a result, within our realistic
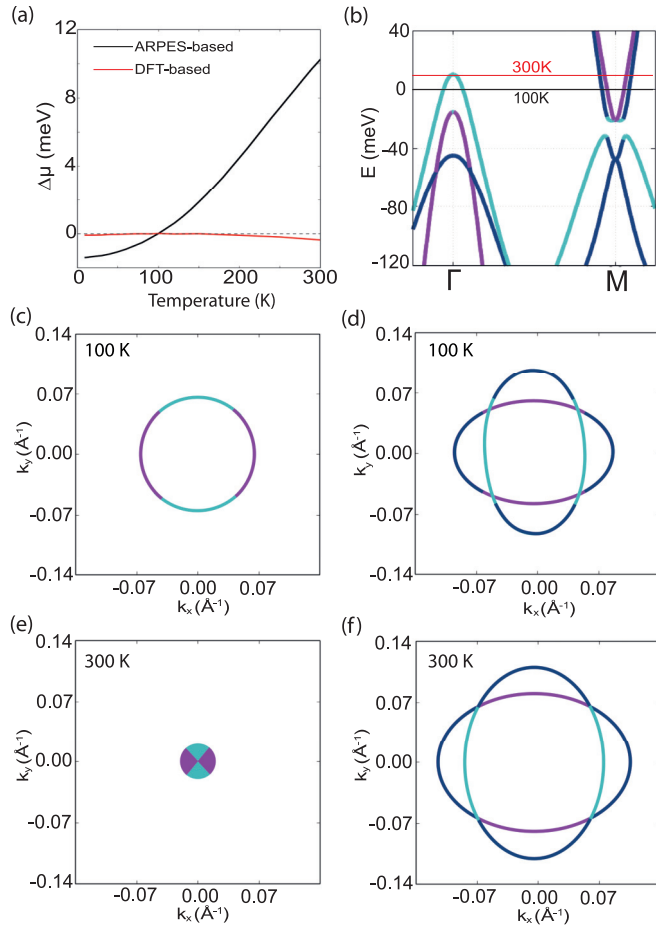
FIG. 2. Predicted temperature effects of the chemical potential in FeSe. (a) Chemical potential as a function of temperature predicted using our ARPES-based parameters (black line), compared to a set of DFT-based parameters (red line). (b) Band dispersions along Γ-M indicating the location of the chemical potential at 100 and 300 K. (c)–(f) The corresponding Fermi surface maps for the hole (left) and electron (right) pocket at 100 K (c,d) and 300 K (e,f).

ARPES-based parameter set we find a nontrivial chemical potential effect, particularly for temperatures exceeding 100 K.

As the top of the hole band at Γ is $\sim$10 meV above the chemical potential, a shift as large as we predict would cause a substantial change to the Fermi surface topology. In Fig. 2(b) we show where the chemical potential would cut the band structure at 100 and 300 K. By 300 K the chemical potential would just be touching the top of the hole band at Γ. The effect of this on the Fermi surface is shown in Figs. 2(c)–2(f). The chemical potential increase would lead to a dramatic reduction of the k_F value of the hole pocket as a function of temperature, and an increase of the k_F value of the electron pocket.

B. Chemical potential shifts in ARPES measurements

To confirm the predicted temperature dependence of the chemical potential, we tracked the evolution of the hole and electron pockets at the high-symmetry Z and A points by ARPES.

In Fig. 3 we show the temperature dependence of the hole (Z point) and electron (A point) pockets as a function of temperature. At 100 K the hole pocket has two circular bands crossing the chemical potential, as described by our ARPES-based parameters for the Z point. The electron pocket is composed of two overlapping ellipses, roughly the same size as the hole pocket. As the temperature is increased, we observe a shrinking of the hole pocket and growth of the electron pocket, consistent with a rigid shift of the chemical potential as seen in other iron-based superconductors and described by our model.

By $\sim$200 K, the inner hole band at the hole pocket shifts below the chemical potential, followed by the outer hole pocket by $\sim$300 K, suggesting multiple temperature-induced Lifshitz transitions [29]. The electron pocket grows monotonically and appears more circular by 300 K, which can be explained by the different Fermi velocities of the two overlapping electron bands, and has been observed in K-doped systems [30].

To determine the magnitude of the chemical potential shift, we analyze the change of peak positions in the energy distribution curves (EDCs). In Figs. 4(a) and 4(b) we plot the EDCs for the centers of the hole and electron pockets, respectively, as a function of temperature. For the hole pockets, two main features are observed: the intense d_{z^2} peak at $\sim$220 meV, and a complex peak close to the chemical potential, which arises from the overlap of d_{xz}, d_{yz}, and d_{xy} bands. For the electron pockets, the EDC has a single peak that originates from the slightly overlapping d_{xz}/d_{yz} and d_{xy} bands [14]. It can be seen from both Figs. 4(a) and 4(b) that the peak positions shift linearly as a function of temperature for all bands, further confirming a rigid band shift of the chemical potential. By extracting the peak position for the d_{z^2} band in Fig. 4(a), which is composed of only a single feature and is situated far away from the chemical potential, we obtain a linear decrease of $\sim$ -0.13 meV/K leading to a rigid band shift of $\sim$25 meV between 100 and 300 K.

In Fig. 4(c) we plot the experimentally extracted k_F values as a function of temperature for the hole pockets. To obtain the k_F values, we fit the 100 K MDC at the Fermi level with a $\pm$1 meV integration window with two pairs of Lorentzian functions. We then relax the peak positions of these Lorentzian functions and fit to higher-temperature data. Assuming that the chemical potential shift is proportional to temperature, and that the hole band dispersions are quadratic, we should expect to observe a square root behavior of k_F as a function of temperature. The square root functions fitted to the data (blue lines) show that the k_F values for both the inner and outer hole bands are in agreement with this assumption and suggest that the entire hole pocket has shifted below the chemical potential by $\sim$300 K. We also present the k_F values of the electron pockets as a function of temperature in Fig. 4(d). For the electron pockets, the band dispersions in the vicinity of the chemical potential are approximately linear, as seen in Fig. 1. As a result, the increase in the chemical potential leads to linear increases in k_F values. The different Fermi velocities of the two overlapping electron pockets are also apparent from the different slopes of the linear fits to the k_F values. All the experimental results point toward a rigid increase of the chemical potential across the entire Brillouin zone.
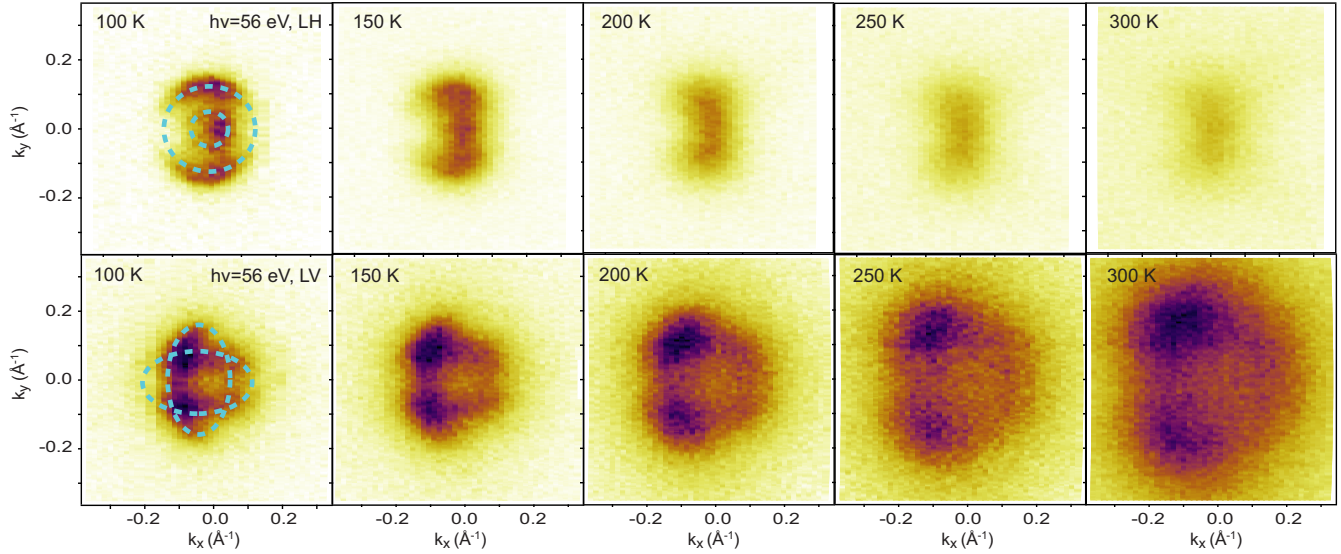
FIG. 3. Temperature-dependent Fermi surfaces of the hole pocket (top row) and electron pocket (bottom row), taken at a photon energy of 56 eV between 100 and 300 K. ARPES intensity was integrated within a ±5 meV range around the Fermi level. The axes are defined relative to the center of the pocket.

V. DISCUSSION

While the ARPES-based parameter set predicts a significant temperature dependence of the chemical potential between 100 and 300 K (10 meV), the experimentally observed shift appears to be over twice as large (25 meV). Although there could be some limitations to the precision of our model, the most important features that affect the chemical potential shift, namely the position of the top of the hole band and the bottom of the electron band with respect to the chemical potential, are very accurate for the experimental quasiparticle dispersions at 100 K. It does not seem likely that the enhancement of the

chemical potential shift by a factor of 2 is due to any numerical inaccuracy of the model.

We are thus led to the conclusion that this discrepancy must be attributed to temperature-dependent electronic correlations, which are not accounted for in our tight-binding model. Such correlations could lead to a reduction in the quasiparticle coherent weight with increasing temperature, as well as temperature-dependent lifetime effects and possibly to asymmetric spectral line shapes. In particular, a decrease in the quasiparticle coherent weight with increasing temperature would lead to a decrease in the density of states, which would require a greater increase in the chemical potential
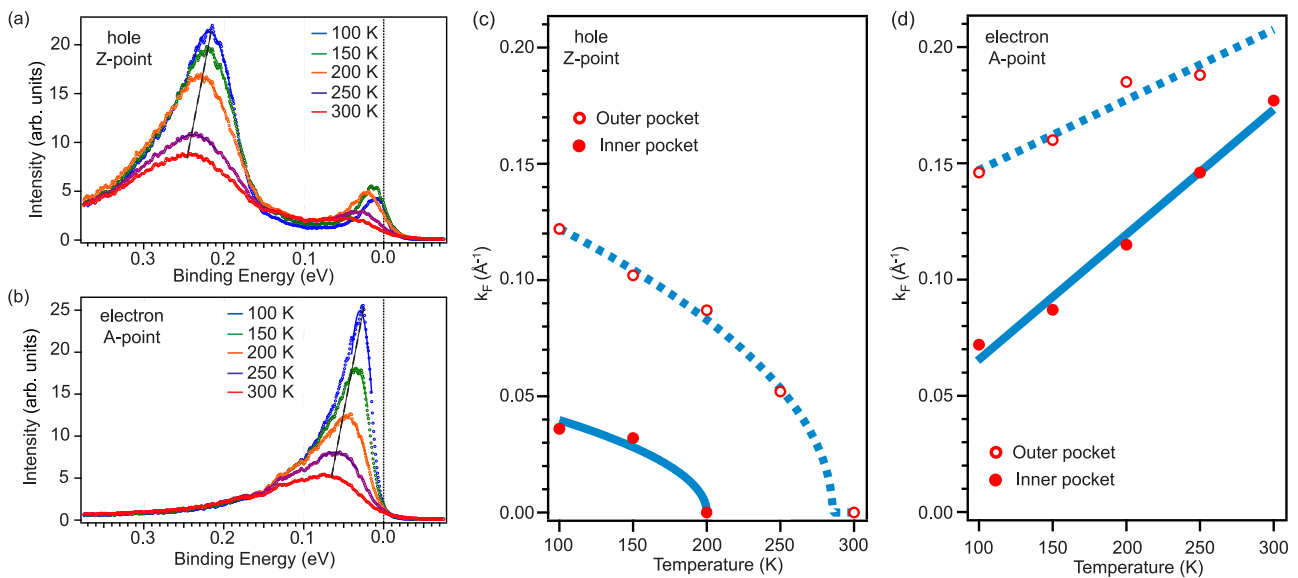

FIG. 4. Energy distribution curves for the center of the hole (a) and electron (b) pockets as a function of temperature. (c,d) Measured k_F values extracted from the fit to the momentum distribution curves at the Fermi level as a function of temperature, for the hole and electron point, respectively. A square root fit was used for the trendline of (c) while a linear fit was used for (d).

to compensate for the extra loss of states. Such effects are often described in terms of self-energy effects, and have been discussed previously in theoretical studies of iron pnictides [31,32].

Notable increases to the chemical potential as a function of temperature have already been observed in other iron-based superconductors [26–28]. This effect is pronounced in FeSe due to the particularly small Fermi surface pockets. Thus the Fermi surface of FeSe at 300 K, with only the electron bands crossing the chemical potential, is qualitatively different from the familiar picture of hole and electron pockets, as observed at 100 K.

The large temperature dependence of the chemical potential in the range of 100–300 K has important implications for the understanding of various physical properties of FeSe, particularly transport measurements and the spin fluctuation spectrum as probed by inelastic neutron scattering. Specifically, the chemical potential shift at high temperatures will result in worse Fermi surface nesting properties between the hole and electron pockets, which could be relevant to the suppression of $(\pi,0)$ magnetic fluctuations at temperatures above 100 K [33]. The chemical potential will also play a role at the nematic transition at 90 K, since any orbital order parameter that creates band shifts around the Fermi level will necessitate a shift of the chemical potential to preserve the total charge of the system. Thus the recently observed momentum-independent downward shift of the d_{xy} band observed below 90 K [14,34] could be interpreted as being primarily a chemical potential effect.

VI. SUMMARY

To conclude, we have determined a set of tight-binding parameters for the high-temperature tetragonal phase of FeSe that is in good quantitative agreement with high-resolution ARPES data at 100 K. We have used these parameters to

predict a large temperature dependence of the chemical potential in FeSe that is not captured from DFT-based parameters. We have performed a temperature-dependent ARPES study of FeSe up to room temperature and observed an enhanced 25 meV shift of the chemical potential between 100 and 300 K. Our study provides a quantitatively accurate description of the low-energy quasiparticle dispersions, and it highlights the necessity for full consideration of the chemical potential in future studies of FeSe.

Note added. During preparation of this publication, we became aware of a similar temperature-dependent study of FeSe by Kushnirenko *et al.* [35]. We are in agreement with Kushnirenko *et al.* with regard to the shifts at the electron pockets, both observing a temperature-dependent downward shift of ~ 25 meV between 100 and 270 K. However, our observations disagree with their claim of an increase in the size of the hole pocket.

APPENDIX

1. Tight-binding optimization

Starting from the renormalized tight-binding parameters from Ref. [22], we optimize the 28 2D and 17 3D tight-binding parameters to the experimentally extracted band dispersions by a least-squares method using the Powell optimization
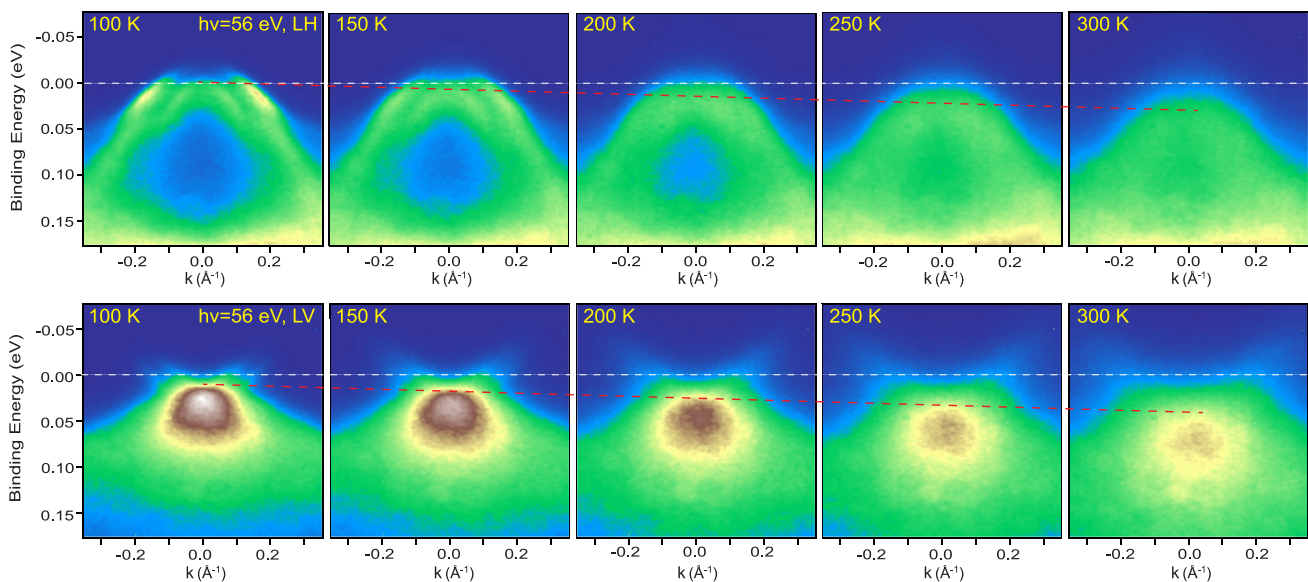

FIG. 5. Temperature-dependent high-symmetry band dispersions of the hole (top row) and electron (bottom row) pockets, taken with a photon energy of 56 eV corresponding to the Fermi surface maps in Fig. 3.

algorithm [36]. Following the notation of Ref. [19], we label the hopping parameters as $t_{\alpha\beta}^{xy}$, where x and y denote the real-space Fe-Fe hopping in the x and y directions of the quasi-2D plane, and α,β denote the initial and final orbital that the hopping parameter is describing. ϵ_α describes the on-site energy of orbital α. The orbitals are numbered as [$1 : d_{xy}^+, 2 : d_{x^2-y^2}^+, 3 : id_{xz}^+, 4 : id_{yz}^+, 5 : d_{z^2}^+, 6 : d_{xy}^-, 7 : d_{x^2-y^2}^-, 8 : -id_{xz}^-, 9 : -id_{yz}^-, 10 : d_{z^2}^-$], where the $+$ and $-$ indicate whether the orbital is on Fe site 1 or 2. $\mu(100\,\text{K})$ is the chemical potential at 100 K, and λ_{SOC} is the magnitude of the spin-orbit coupling used in the model. While most parameters are only altered by less than $\pm 30\%$, there are significant changes (over 100%) in $t_{11}^{20}, t_{16}^{21}, t_{49}^{21}$, and ϵ_1.

The hopping parameters obtained from the optimization are as follows:

2D parameters

$t_{11}^{11} = 0.01818$	$t_{16}^{10} = -0.03133$	$t_{33}^{11} = 0.02433$
$t_{11}^{20} = 0.00093$	$t_{16}^{21} = -0.00231$	$t_{33}^{20} = 0.00096$
$t_{13}^{11} = -0.01226i$	$t_{18}^{10} = 0.11516i$	$t_{33}^{02} = -0.00717$
$t_{15}^{11} = -0.01817$	$t_{27}^{10} = -0.04988$	$t_{33}^{22} = 0.00758$
$t_{22}^{11} = -0.01669$	$t_{29}^{10} = -0.09492i$	$t_{38}^{10} = 0.00868$
$t_{23}^{11} = 0.01484i$	$t_{2,10}^{10} = 0.059659$	$t_{38}^{21} = -0.00493$
$t_{34}^{11} = 0.01650$	$t_{35}^{11} = 0.00569i$	$t_{4,10}^{10} = -0.00902i$

$t_{49}^{10} = 0.05023$	$t_{49}^{21} = -0.00008$	
$\epsilon_1 = 0.03405$	$\epsilon_2 = -0.05050$	$\epsilon_3 = 0.00310$
$\epsilon_4 = 0.00310$	$\epsilon_5 = -0.19398$	
$\mu(100\,\text{K}) = 0.012$	$\lambda_{\text{SOC}} = 0.016$	

3D parameters

$t_{16}^{101} = 0.00270$	$t_{11}^{001} = 0$	$t_{14}^{201} = 0.00950i$
$t_{16}^{121} = -0.00283$	$t_{11}^{111} = 0$	$t_{19}^{101} = 0.00333i$
$t_{18}^{101} = 0.00150i$	$t_{11}^{201} = 0.00013$	$t_{19}^{121} = 0.00517i$
$t_{33}^{001} = 0.00183$	$t_{38}^{101} = 0.00300$	$t_{49}^{121} = 0.00100.$
$t_{33}^{201} = -0.00133$	$t_{38}^{121} = -0.00050$	$t_{49}^{101} = 0.00217$
$t_{33}^{021} = 0.00333$	$t_{39}^{101} = 0.00250$	

2. Band dispersions

In Fig. 5 we present the band dispersions corresponding to the high-symmetry cuts of Fig. 3. The white dashed line is the chemical potential position. A rigid shift of both the hole and electrons bands is observed, consistent with an increase of the chemical potential.

[1] A. I. Coldea, J. D. Fletcher, A. Carrington, J. G. Analytis, A. F. Bangura, J.-H. Chu, A. S. Erickson, I. R. Fisher, N. E. Hussey, and R. D. McDonald, Fermi Surface of Superconducting Lafepo Determined from Quantum Oscillations, Phys. Rev. Lett. **101**, 216402 (2008).

[2] H. Ding, K. Nakayama, P. Richard, S. Souma, T. Sato, T. Takahashi, M. Neupane, Y-M. Xu, Z-H. Pan, A. V. Fedorov, Z. Wang, X. Dai, Z. Fang, G. F. Chen, J. L. Luo, and N. L. Wang, Electronic structure of optimally doped pnictide Ba$_{0.6}$K$_{0.4}$Fe$_2$As$_2$: A comprehensive angle-resolved photoemission spectroscopy investigation, J. Phys. Condens. Matter **23**, 135701 (2011).

[3] K. Nakayama, T. Sato, P. Richard, T. Kawahara, Y. Sekiba, T. Qian, G. F. Chen, J. L. Luo, N. L. Wang, H. Ding, and T. Takahashi, Angle-Resolved Photoemission Spectroscopy of the Iron-Chalcogenide Superconductor Fe$_{1.03}$Te$_{0.7}$Se$_{0.3}$: Strong Coupling Behavior and the Universality of Interband Scattering, Phys. Rev. Lett. **105**, 197001 (2010).

[4] Z. P. Yin, K. Haule, and G. Kotliar, Kinetic frustration and the nature of the magnetic and paramagnetic states in iron pnictides and iron chalcogenides, Nat. Mater. **10**, 932 (2011).

[5] M. Aichhorn, S. Biermann, T. Miyake, A. Georges, and M. Imada, Theoretical evidence for strong correlations and incoherent metallic state in FeSe, Phys. Rev. B **82**, 064504 (2010).

[6] M. D. Watson, S. Backes, A. A. Haghighirad, M. Hoesch, T. K. Kim, A. I. Coldea, and R. Valentí, Formation of Hubbard-like bands as a fingerprint of strong electron-electron interactions in FeSe, Phys. Rev. B **95**, 081106 (2017).

[7] F. C. Hsu, J. Y. Luo, K. W. Yeh, T. 0K. Chen, T. W. Huang, P. M. Wu, Y. C. Lee, Y. L. Huang, Y. Y. Chu, D. C. Yan, and M. K. Wu, Superconductivity in the PbO-type structure of α-FeSe, Proc. Natl. Acad. Sci. (U.S.A.) **105**, 14262 (2008).

[8] S. Medvedev, T. M. McQueen, I. A. Troyan, T. Palasyuk, M. I. Eremets, R. J. Cava, S. Naghavi, F. Casper, V. Ksenofontov, G. Wortmann, and C. Felser, Electronic and magnetic phase diagram of β-Fe$_{1.01}$Se with superconductivity at 36.7 K under pressure, Nat. Mater. **8**, 630 (2009).

[9] M. Burrard-Lucas, D. G. Free, S. J. Sedlmaier, J. D. Wright, S. J. Cassidy, Y. Hara, A. J. Corkett, T. Lancaster, P.J. Baker, S. J. Blundell, and S. J. Clarke, Enhancement of the superconducting transition temperature of FeSe by intercalation of a molecular spacer layer, Nat. Mater. **12**, 15 (2013).

[10] S. He, J. He, W. Zhang, L. Zhao, D. Liu, X. Liu, D. Mou, Y-B. Ou, Q-Y. Wang, Z. Li, L. Wang, Y. Peng, Y. Liu, C. Chen, L. Yu, G. Liu, X. Dong, J. Zhang, C. Chen, Z. Xu, X. Chen, X. Ma, Q. Xue, and X. J. Zhou, Phase diagram and electronic indication of high-temperature superconductivity at 65 K in single-layer FeSe films, Nat. Mater. **12**, 605 (2013).

[11] R. M. Fernandes, A. V. Chubukov, and J. Schmalian, What drives nematic order in iron-based superconductors? Nat. Phys. **10**, 97 (2014).

[12] S. V. Borisenko, D. V. Evtushinsky, Z.-H Liu, I. Morozov, R. Kappenberger, S. Wurmehl, B. Büchner, A. N. Yaresko, T. K. Kim, M. Hoesch, T. Wolf, and N. D. Zhigadlo, Direct observation of spin-orbit coupling in iron-based superconductors, Nat. Phys. **12**, 311 (2016).

[13] M. D. Watson, T. K. Kim, A. A. Haghighirad, N. R. Davies, A. McCollam, A. Narayanan, S. F. Blake, Y. L. Chen, S. Ghannadzadeh, A. J. Schofield, M. Hoesch, C. Meingast, T. Wolf, and A. I. Coldea, Emergence of the nematic electronic state in FeSe, Phys. Rev. B **91**, 155106 (2015).

[14] M. D. Watson, T. K. Kim, L. C. Rhodes, M. Eschrig, M. Hoesch, A. A. Haghighirad, and A. I. Coldea, Evidence for unidirectional nematic bond ordering in FeSe, Phys. Rev. B **94**, 201107 (2016).

[15] A. Fedorov, A. Yaresko, T. K. Kim, Y. Kushnirenko, E. Haubold, T. Wolf, M. Hoesch, A. Grneis, B. Büchner, and S. V. Borisenko, Effect of nematic ordering on electronic structure of FeSe, Sci. Rep. **6**, 36834 (2016).

[16] L. Fanfarillo, J. Mansart, P. Toulemonde, H. Cercellier, P. Le Fèvre, F C. Bertran, B. Valenzuela, L. Benfatto, and V. Brouet, Orbital-dependent Fermi surface shrinking as a fingerprint of nematicity in FeSe, Phys. Rev. B **94**, 155138 (2016).

[17] A. E. Böhmer, F. Hardy, F. Eilers, D. Ernst, P. Adelmann, P. Schweiss, T. Wolf, and C. Meingast, Lack of coupling between superconductivity and orthorhombic distortion in stoichiometric single-crystalline FeSe, Phys. Rev. B **87**, 180505 (2013).

[18] M. Hoesch, T. K. Kim, P. Dudin, H. Wang, S. Scott, P. Harris, S. Patel, M. Matthews, D. Hawkins, S. G. Alcock, T. Richter, J. J. Mudd, M. Basham, L. Pratt, P. Leicester, E. C. Longhi, A. Tamai, and F. Baumberger, A facility for the analysis of the electronic structures of solids and their surfaces by synchrotron radiation photoelectron spectroscopy, Rev. Sci. Instrum. **88**, 013106 (2017).

[19] H. Eschrig and K. Koepernik, Tight-binding models for the iron-based superconductors, Phys. Rev. B **80**, 104503 (2009).

[20] T. Saito, Y. Yamakawa, S. Onari, and H. Kontani, Revisiting orbital-fluctuation-mediated superconductivity in LiFeAs: Non-trivial spin-orbit interaction effects on the band structure and superconducting gap function, Phys. Rev. B **92**, 134522 (2015).

[21] S. Graser, A. F. Kemper, T. A. Maier, H.-P. Cheng, P. J. Hirschfeld, and D. J. Scalapino, Spin fluctuations and superconductivity in a three-dimensional tight-binding model for $BaFe_2As_2$, Phys. Rev. B **81**, 214503 (2010).

[22] S. Mukherjee, A. Kreisel, P. J. Hirschfeld, and B. M. Andersen, Model of Electronic Structure and Superconductivity in Orbitally Ordered FeSe, Phys. Rev. Lett. **115**, 026402 (2015).

[23] O. K. Andersen and L. Boeri, On the multi-orbital band structure and itinerant magnetism of iron-based superconductors, Ann. Phys. (Berlin) **523**, 8 (2011).

[24] E. M. Nica, R. Yu, and Q. Si, Glide reflection symmetry, Brillouin zone folding, and superconducting pairing for the $P4/nmm$ space group, Phys. Rev. B **92**, 174520 (2015).

[25] N. Hao and J. Hu, Topological Phases in the Single-Layer FeSe, Phys. Rev. X **4**, 031053 (2014).

[26] V. Brouet, P-H. Lin, Y. Texier, J. Bobroff, A. Taleb-Ibrahimi, P. Le Fèvre, F. Bertran, M. Casula, P. Werner, S. Biermann, F. Rullier-Albenque, A. Forget, and D. Colson, Large Temperature Dependence of the Number of Carriers in Co-Doped $BaFe_2As_2$, Phys. Rev. Lett. **110**, 167002 (2013).

[27] R. S. Dhaka, S. E. Hahn, E. Razzoli, R Jiang, M. Shi, B. N. Harmon, A. Thaler, S. L. Bud'ko, P. C. Canfield, and A. Kaminski, Unusual Temperature Dependence of Band Dispersion in $Ba(Fe_{1-x}Ru_x)_2As_2$ and its Consequences for Antiferromagnetic Ordering, Phys. Rev. Lett. **110**, 067002 (2013).

[28] M. Abdel-Hafiez, Y. J. Pu, J. Brisbois, R. Peng, D. L. Feng, D. A. Chareev, A. V. Silhanek, C. Krellner, A. N. Vasiliev, and X.-J. Chen, Impurity scattering effects on the superconducting properties and the tetragonal-to-orthorhombic phase transition in FeSe, Phys. Rev. B **93**, 224508 (2016).

[29] Y. Wu, N. H. Jo, M. Ochi, L. Huang, D. Mou, S. L. Bud'ko, P. C. Canfield, N. Trivedi, R. Arita, and A. Kaminski, Temperature-Induced Lifshitz Transition in WTe_2, Phys. Rev. Lett. **115**, 166602 (2015).

[30] Y. Miyata, K. Nakayama, K. Sugawara, T. Sato, and T. Takahashi, High-temperature superconductivity in potassium-coated multilayer FeSe thin films, Nat. Mater. **14**, 775 (2015).

[31] A. Heimes, R. Grein, and M. Eschrig, Electronic Dispersion Anomalies in Iron Pnictide Superconductors, Phys. Rev. Lett. **106**, 047003 (2011).

[32] A. Heimes, R. Grein, and M. Eschrig, Effect of spin fluctuations on the electronic structure in iron-based superconductors, Phys. Rev. B **86**, 064528 (2012).

[33] Q. Wang, Y. Shen, B. Pan, X. Zhang, K. Ikeuchi, K. Iida, A. D. Christianson, H. C. Walker, D. T. Adroja, M. Abdel-Hafiez, X. Chen, D. A. Chareev, A. N. Vasiliev, and J. Zhao, Magnetic ground state of FeSe, Nat. Commun. **7**, 12182 (2016).

[34] M. D. Watson, A. A. Haghighirad, H. Takita, W. Mansur, H. Iwasawa, E. F. Schwier, A. Ino, and M. Hoesch, Shifts and splittings of the hole bands in the nematic phase of FeSe, J. Phys. Soc. Jpn. **86**, 053703 (2017).

[35] Y. Kushnirenko, A. A. Kordyuk, A. Fedorov, E. Haubold, T. Wolf, B. Büchner, and S. V. Borisenko, Anomalous temperature evolution of the electronic structure of FeSe, arXiv:1702.02088.

[36] W. H. Press, S. A. Teukolsky, W. T. Vetterling, and B. P. Flannery, *Numerical Recipes in Fortran 90*, 2nd ed. (Cambridge University Press, Cambridge, 1996).